Optics Letters

On-chip non-uniform geometric metasurface for multi-channel wavefront manipulations

Bin Fang,[1,4,†] Fangzhou Shu,[1,†] Zhizhang Wang,[2] Jitao Ji,[2] Zhongwei Jin,[1] Zhi Hong,[1] Changyu Shen,[1] Qingqing Cheng,[3] and Tao Li[2,5]

[1]College of Optical and Electronic Technology, Centre for THz Research, China Jiliang University, Hangzhou 310018, China
[2]National Laboratory of Solid State Microstructures, College of Engineering and Applied Sciences, Nanjing University, Nanjing 210093, China
[3]School of Optical-Electrical and Computer Engineering, University of Shanghai for Science and Technology, Shanghai 200093, China
[4]binfang@cjlu.edu.cn
[5]taoli@nju.edu.cn
[†]These authors contributed equally to this work.

Received 22 February 2023; revised 19 April 2023; accepted 5 May 2023; posted 8 May 2023; published 1 June 2023

Metasurfaces integrated with waveguides have been recently explored as a means to control the conversion between guided modes and radiation modes for versatile functionalities. However, most efforts have been limited to constructing a single free-space wavefront using guided waves, which hinders the functional diversity and requires a complex configuration. Here, a new, to the best of our knowledge, type of non-uniformly arranged geometric metasurface enabling independent multi-channel wavefront engineering of guided wave radiation is ingeniously proposed. By endowing three structural degrees of freedom into a meta-atom, two mechanisms (the Pancharatnam–Berry phase and the detour phase) of the metasurface are perfectly joined together, giving rise to three phase degrees of freedom to manipulate. Therefore, an on-chip polarization demultiplexed metalens, a wavelength-multiplexed metalens, and RGB-colored holography with an improved information capacity are successively demonstrated. Our results enrich the functionalities of an on-chip metasurface and imply the prospect of advancements in multiplexing optical imaging, augmented reality (AR) holographic displays, and information encryption.

https://doi.org/10.1364/OL.488475

Optical waveguide technology is one of the most promising approaches for producing future high-performance and compact optoelectronic devices for light detection and ranging (lidar) [1] and augmented reality (AR)/virtual reality (VR) displays [2]. Typically, the conversion between and manipulation of guided wave and radiation modes play a key role in versatile off-chip performance. However, the traditional coupling interface that bridges them employs grating structures [3], which have a large footprint, high-order diffraction loss, and lack complete control of the scattered electromagnetic waves. Metasurfaces consisting of subwavelength optical antennas have newly emerged as artificially designed electromagnetic interfaces [4]. With an unparalleled capability for engineering the phase, amplitude, and polarization of light at the subwavelength scale, they provide a powerful platform for various applications in wavefront shaping, metalens imaging, and holography displays [5–9].

Although typical metasurfaces focus on controlling the wavefront of light propagating in free space, metasurface concepts have recently advanced in the field of integrated photonics [10], including on-chip light coupling [11], mode conversion [12], frequency conversion [13], and, very recently, the generation of wavefronts motivated by in-plane guided modes [14–20]. For instance, off-chip beam deflection and focusing was demonstrated by exploiting the collective resonant effect of a uniformly arranged metasurface patterned on a waveguide, which leveraged two degrees of freedom (the length and width of the meta-atom) to control the phase profile of scattered light [14]. As an alternative, a robust and easily implemented uniform geometric metasurface interface based on the Pancharatnam–Berry (PB) phase was also developed to mold the guided wave into free-space functional beams but with a single degree of manipulation freedom [19]. In general, the fundamental design of a metasurface depends on the local wave modulation enabled by varying the size (resonant phase or propagation phase) [21,22] and rotation angle (PB phase or geometric phase) of the uniformly arranged meta-atoms. However, the former relies on complex optimizations of multiple parameters, and the latter is subject to the locked phase response of opposite spins, and both of which hinder the practical multiplexing capacity. Therefore, further research on independent multi-channel multiplexing technology operating on-chip modes is highly expected.

In this work, we develop an on-chip non-uniformly arranged geometric metasurface interface for guided wave radiation manipulation, which enables independent multi-functional wavefront engineering in the visible regime. By introducing three structural degrees of freedom into a meta-atom, namely the displacement along the x and y directions as well as the rotation angle, two mechanisms—the PB phase and the detour phase [23,24]—introduced by the metasurface are perfectly combined, giving rise to three phase degrees of freedom to control. Therefore, the spin-correlated phase response of a geometric metasurface can be broken, and a polarization demultiplexed metalens as well as a wavelength multiplexed metalens

integrated with a waveguide is firstly demonstrated for bifunctional manipulations, with a polarization extinction ratio of over 14.5 dB. Subsequently, by encoding three wavelengths to three phase profiles, a more ingenious metasurface is implemented to construct an off-chip RGB-colored hologram with respect to two incident directions of guided waves. Our proposal takes full advantage of the on-chip geometric metasurface, expanding the information channel capacity, and could provide a new platform to produce multiplexed metadevices for imaging, AR holographic displays, or information encryption.

Starting from a simple case, we consider a transverse-electric (TE) guided mode, which resembles a superposition of waves with right-hand circular polarization (RCP) and waves with left-hand circular polarization (LCP) propagating along the x direction inside a slab waveguide with a propagation constant β. The geometric metasurface nanoantennas on top of the slab waveguide can then be regarded as a series of subsources radiating a small portion of the guided wave into free space with LCP and RCP, with phase lags $\phi(x, y) = \phi_{DP}(x, y) + \sigma\phi_{PB}(x, y)$ imposed [19]. Here, $\phi_{PB}(x, y) = 2\theta$ is the PB phase profile determined by the meta-atoms' orientation θ, and σ represents two different spin states of the radiated CP wave. Meanwhile, $\phi_{DP}(x, y) = \beta x$ is the detour phase, a spin-independent but path-related basic phase shift originating from the optical path length difference of the light. It should be noted that we ignore the co-polarization wave since we can employ a metasurface with high polarization conversion efficiency (PCE). For a conventional uniformly arranged geometric metasurface [see Fig. 1(a)], once the period of the metasurface is settled upon, the location of each meta-atom is fixed. Then $\phi_{DP}(x, y)$ performs as a linear gradient phase, which only influences the output angle of the extracted beam due to momentum conservation, while providing one degree of freedom θ to control the phase profile. Unfortunately, PB phase responses of two opposite spin components are essentially locked with the inverse phase profile, limiting the function multiplexing. Therefore, we introduce the concept of a non-uniform metasurface [see Fig. 1(b)], where the detour phase is regarded as a new degree of freedom combined with the PB phase to break the spin-correlated functional response. Specifically, the phase lags determined by the metasurface for radiated LCP and RCP waves can be described as

$$\begin{bmatrix} \phi_L(x,y) \\ \phi_R(x,y) \end{bmatrix} = \beta x \begin{bmatrix} 1 \\ 1 \end{bmatrix} + 2\theta \begin{bmatrix} 1 \\ -1 \end{bmatrix}. \quad (1)$$

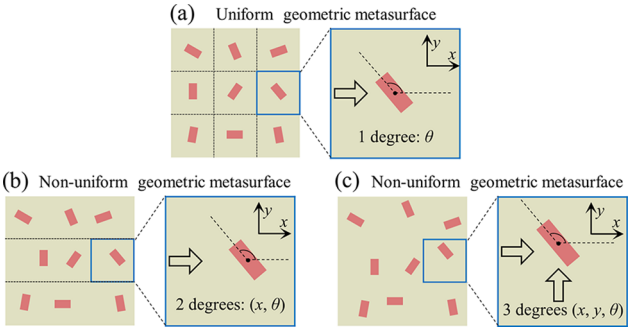

Fig. 1. Working principle of on-chip geometric metasurfaces. Schematic depiction of (a) uniformly arranged metasurfaces with one degree of freedom θ, (b) non-uniformly arranged metasurfaces with two degrees of freedom (x, θ), and (c) non-uniformly arranged metasurfaces with three degrees of freedom (x, y, θ) to manipulate guided wave radiation.

As a result, two independent wavefront modulations can be offered by simply adjusting the two degrees of freedom (x, θ). Furthermore, if we consider two guided modes injected into the slab waveguide from two orthogonal ports [see Fig. 1(c)], the detour phase in the y direction offers another degree of freedom to manipulate the extracted y-polarized guided wavefront, as summarized by the following equation:

$$\begin{bmatrix} \phi_L(x,y) \\ \phi_R(x,y) \\ \phi_y(x,y) \end{bmatrix} = \beta x \begin{bmatrix} 1 \\ 1 \\ 0 \end{bmatrix} + \beta y \begin{bmatrix} 0 \\ 0 \\ 1 \end{bmatrix} + 2\theta \begin{bmatrix} 1 \\ -1 \\ 0 \end{bmatrix}. \quad (2)$$

At this point, by merging the local PB phase of geometric metasurfaces and the detour phase, three structural parameters (x, y, θ) are mapped to three phase degrees of freedom, enabling trifunctional wavefront manipulations.

For a demonstration, we firstly introduce a polarization-demultiplexed metalens for dual-functional manipulation. Earlier work revealed that a uniformly arranged geometric metasurface can conveniently extract the guided wave and cause it to converge at a designed focal point with LCP, while it turns divergent for an RCP wave [19]. To break such a spin-locked phase correlation, inhomogeneous detour phase distributions achieved by individually designing the locations of the local meta-atoms in the x direction are adopted, leading to two distinct lens phase profiles for the extracted LCP and RCP waves [as schematically shown in Fig. 2(a)]. The detailed designs are as follows. At the operating wavelength $\lambda = 700$ nm, the amorphous silicon (α-Si) metasurfaces convert the TE_0 guided mode of the lithium-niobate-on-insulator (LNOI) slab waveguide (thickness = 300 nm) into LCP free-space light which is focused at (−2.5, 0, 16 μm) and into RCP light focused at (2.5, 0, 16 μm). The rectangular nanoantenna has an arm length $L = 100$ nm, arm width $W = 60$ nm, and height $H = 300$ nm. Here we take LNOI as an ideal waveguide platform and Si as an optimal metasurface interface due to their widespread and mature applications in integrated photonics. The high refractive index contrast between them also allows high extraction efficiency. As a proof of concept, we numerically simulate a 2D metalens (diameter $D = 10$ μm) using finite-difference-time-domain software (FDTD Solutions) from Lumerical Inc. Based on Eq. (1), we obtain the parameters (x, θ) of each nanorod while the period along the y propagation direction is fixed at 200 nm, and then we construct the devices. Figures 2(b) and 2(c) show the simulated intensity distributions of the radiated LCP wave and RCP wave in the x-z plane, respectively, where the TE_0 mode is injected into the slab waveguide from its left port. The simulation results reveal that the LCP light is focused to a focal point (−2.5, 0, 16 μm) above the slab waveguide, and the RCP light is simultaneously focused on another point (2.44, 0, 16 μm), which agrees well with the designs. The intensity distributions at the focal plane manifest a near-diffraction-limited Airy disk [Figs. 2(d) and 2(e)] with a full width at half-maximum (FWHM) of about 1.23 μm and 1.21 μm [Fig. 2(f)]. For a quantitative analysis of the polarization demultiplexing performance of the spin-decoupled metalens, we calculate the polarization extinction ratio (PER), defined as the ratio of the electric-field intensities of the two orthogonal polarization components at the focus point. The corresponding PER is around 15.5 dB and 14.5 dB, promising a good signal-to-noise ratio (SNR) [see Fig. 2(g)].

Aside from a polarization demultiplexed metalens, more complex wavelength multiplexed bifunctional wavefront modulations are also demonstrated. Based on the same principle

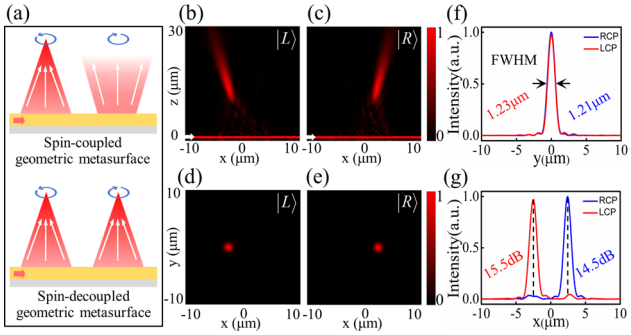

Fig. 2. Demonstration of an on-chip polarization demultiplexed metalens. (a) Schematics of spin-coupled wavefront modulations for traditional PB metasurfaces and the proposed spin-decoupled metasurfaces. (b), (c) Simulated intensity distributions of radiated LCP and RCP waves in the x-z plane at $\lambda = 700$ nm. The light propagates along the x axis from left to right, as shown by the white arrow. (d), (e) The corresponding intensity distributions at the focal plane, showing a near-diffraction-limited Airy disk with (f) a FWHM of about 1.21 μm and 1.23 μm. (g) Intensity distributions of the LCP and RCP waves in the x direction at the focal plane, indicating that the PER at each focal point is 15.5 dB and 14.5 dB, respectively.

as that presented above, we encode two different wavelengths ($\lambda_1 = 435$ nm and $\lambda_2 = 700$ nm) into two phase degrees of freedom according to the revised equation

$$\begin{bmatrix} \phi_{\lambda_1,L}(x,y) \\ \phi_{\lambda_1,R}(x,y) \\ \phi_{\lambda_2,L}(x,y) \\ \phi_{\lambda_2,R}(x,y) \end{bmatrix} = x \begin{bmatrix} \beta_1 \\ \beta_1 \\ \beta_2 \\ \beta_2 \end{bmatrix} + 2\theta \begin{bmatrix} 1 \\ -1 \\ 1 \\ -1 \end{bmatrix}. \quad (3)$$

It should be noted that by carefully controlling the mismatched wave vector, the guided wave imposed with phase lags of $\phi_{\lambda 1,R}$ and $\phi_{\lambda 2,L}$ would not be coupled out, leaving two phase profiles to perform. Figures 3(a)–3(c) show the simulated field intensity distributions in the x-z plane under the excitation of a TE_0 guided wave at $\lambda_1 = 435$ nm propagating in the x direction. We observe that the LCP light scattered out by the metasurface is gradually focused at (−2.1, 0, 20 μm) above the slab waveguide [Fig. 3(a)], and the bare RCP light is scattered out [Figs. 3(b) and 3(c)], which matches our theoretical predictions. The FWHM of the LCP focal spot at 435 nm is 1.01 μm [Fig. 3(d)]. Meanwhile, when the waveguide is excited by another TE_0 mode at $\lambda_2 = 700$ nm propagating in the x direction, almost no LCP light is coupled out, and the scattered RCP light is focused at another focal point (2.0, 0, 20 μm) [Figs. 3(e)–3(g)] with a FWHM of 1.51 μm [Fig. 3(h)]. Judging from the total intensity distributions of the electric field [Figs. 3(c) and 3(g)], we can conclude that the cross talk in such a multiplexing design is small.

To show that more multiplexing capacity is available, we further demonstrate a three-channel multiplexed metasurface interface with an extra degree of encoding freedom for the detour phase in the y direction. Figure 4(a) illustrates the operating scheme of our proposed non-uniform geometric metasurface, which simultaneously enables on-chip three-channel function multiplexing with the independently encoded degrees of freedom (x, y, θ), e.g., RGB-colored meta-holography projections. Specifically, TE guided modes propagating along the x direction are extracted to reconstruct the red flower holographic image with RCP and simultaneously display the blue pot image with

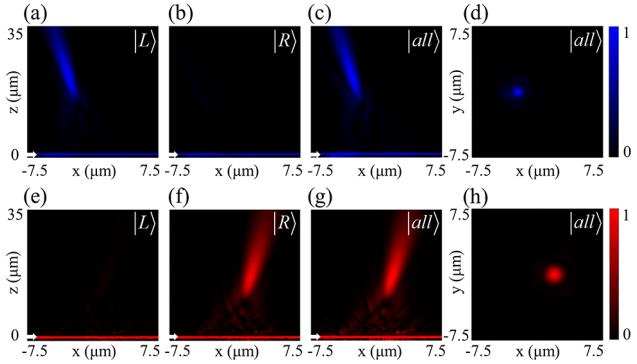

Fig. 3. Numerical simulations of a wavelength multiplexed metalens. (a)–(d) The simulated intensity distributions of the LCP, RCP, and total fields in the x-z plane and x-y plane under the excitation of a TE_0 guided wave at $\lambda_1 = 435$ nm. (e)–(h) The corresponding simulation results at $\lambda_2 = 700$ nm.

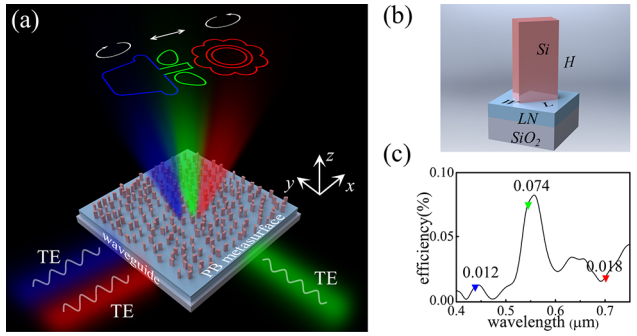

Fig. 4. Triple-channel multiplexed non-uniform geometric metasurface. (a) Schematic of the trifunctional metasurface operating on the on-chip PB phase and detour phase, i.e., generating RGB-colored meta-holography projections. (b) Single metasurface unit with arm length $L = 100$ nm, arm width $W = 60$ nm, and height $H = 300$ nm. (c) The dependence of the extraction efficiency of a metasurface unit on the wavelength.

LCP. Meanwhile, the TE guided wave propagating along the y direction triggers another channel for exhibiting the green peduncle with linear polarization (LP). The single metasurface unit is schematically supplemented in Fig. 4(b). The maximum PCE of the metasurface unit is over 96%, and the extraction efficiencies at 435 nm, 546 nm, and 700 nm are ~ 0.012%, ~ 0.074%, and ~ 0.018%, as shown in Fig. 4(c). Though the efficiency of a single unit is low, the total efficiency is determined by summing over all units, so this could be improved by increasing the number of unit cells that interact with the guided wave as it propagates in the waveguide. Also, we can control the input power ratio of each wavelength to guarantee that the holograms have uniform intensity.

From Eqs. (2) and (3), we firstly derive the database (x, y, θ) of nanorods and create an RGB-color multiplexed metalens. Figures 5(a)–5(c) show the simulated intensity distributions in the x-z plane or y-z plane under the excitation of a TE_0 guided mode at $\lambda_1 = 700$ nm, $\lambda_2 = 546$ nm, and $\lambda_3 = 435$ nm, respectively. Here, the options for the wavelength are based on the 1931 CIE RGB colorimetric system [25], and the pseudocolor provides a guide for the eye for visualizing the different wavelengths. When propagating through the shared metasurface region, the

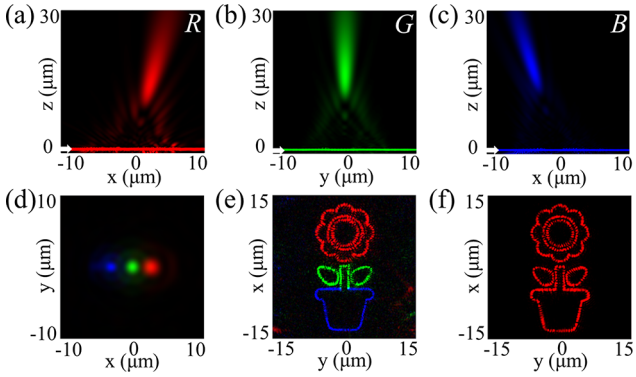

Fig. 5. (a)–(c) Demonstrations of an on-chip multiwavelength multiplexed metalens operating at $\lambda_1 = 700$ nm, $\lambda_2 = 546$ nm, and $\lambda_3 = 435$ nm, respectively. (d) The total intensity distributions at the focal plane under the simultaneous excitation of the three guided modes. (e), (f) Simulated multiwavelength and monochromatic multiplexed holographic images.

extracted light all converges at the designed focal point, with the region behaving as a trifunctional metalens. Figure 5(d) also plots the total intensity distributions at the focal plane under the simultaneous excitation of the three guided modes. For a more general manifestation, more triple-channel colorful holography is demonstrated with the projected figures of a flower, a peduncle, and a pot, achieved under guided illumination from the *x*/*y* direction, as shown in Fig. 5(e). The field intensity distribution is obtained by the vector diffraction method of the near field at $z = 2$ μm as calculated by FDTD. Remarkably, compared with conventional free-space holography, the projected images operating on guided waves are free from zero-order diffraction interference due to the optical on-chip propagation scheme. Meanwhile, the monochromatic ($\lambda = 700$ nm) trichannel multiplexed holographic images are also reconstructed in Fig. 5(f). These have smaller cross talk and higher SNR values than the multi-wavelength holograms.

In conclusion, we have proposed an on-chip, non-uniformly arranged geometric metasurface interface for multi-channel wavefront manipulations of guided wave radiation, with independent encoding freedom. By merging the local PB phase and detour phase of the metasurfaces, three structural parameters are mapped to three phase degrees of freedom, enabling trifunctional multiplexing. As a proof of concept, we firstly demonstrated a polarization demultiplexed metalens based on a non-uniform geometric metasurface in a slab waveguide, followed by a wavelength multiplexed metalens, showing a spin-uncorrelated phase response for bifunctional manipulations. Furthermore, an off-chip RGB-colored hologram with triple-channel wavelength multiplexing technology was presented in detail. We anticipate that the on-chip non-uniform metasurface will offer integrated platform access to multiplexed devices for imaging, AR holographic displays, or information encryption.

Funding. National Natural Science Foundation of China (12204446, 12174186, 12004362, 12174260, 61875179, 12274386); National Key Research and Development Program of China (2022YFA1404301); Key Research and Development plan of Zhejiang Province (2021C01179).

Disclosures. The authors declare no conflicts of interest.

Data availability. Data underlying the results presented in this paper are not publicly available at this time but may be obtained from the authors upon reasonable request.

REFERENCES

1. C. V. Poulton, A. Yaacobi, D. B. Cole, M. J. Byrd, M. Raval, D. Vermeulen, and M. R. Watts, Opt. Lett. **42**, 4091 (2017).
2. D. Cheng, Y. Wang, C. Xu, W. Song, and G. Jin, Opt. Express **22**, 20705 (2014).
3. S. A. Masturzo, J. M. Yarrison-Rice, H. E. Jackson, and J. T. Boyd, IEEE Trans. Nanotechnol. **6**, 622 (2007).
4. N. Yu, P. Genevet, M. A. Kats, F. Aieta, J. Tetienne, F. Capasso, and Z. Gaburro, Science **334**, 333 (2011).
5. Z. L. Deng, M. Jin, X. Ye, S. Wang, T. Shi, J. Deng, N. Mao, Y. Cao, B. O. Guan, A. Alu, G. Li, and X. Li, Adv. Func. Mat. **30**, 1910610 (2020).
6. H. Li, X. Xiao, B. Fang, S. Gao, Z. Wang, C. Chen, Y. Zhao, S. Zhu, and T. Li, Photonics Res. **9**, 1384 (2021).
7. T. Wu, X. Zhang, Q. Xu, E. Plum, K. Chen, Y. Xu, Y. Lu, H. Zhang, Z. Zhang, X. Chen, G. Ren, L. Niu, Z. Tian, J. Han, and W. Zhang, Adv. Opt. Mater. **10**, 2101223 (2022).
8. Q. He, S. Sun, S. Xiao, and L. Zhou, Adv. Opt. Mater. **6**, 1800415 (2018).
9. N. A. Rubin, Z. Shi, and F. Capasso, Adv. Opt. Photonics **13**, 836 (2021).
10. Y. Meng, Y. Chen, L. Lu, Y. Ding, A. Cusano, J. A. Fan, Q. Hu, K. Wang, Z. Xie, Z. Liu, Y. Yang, Q. Liu, M. Gong, Q. Xiao, S. Sun, M. Zhang, X. Yuan, and X. Ni, Light: Sci. Appl. **10**, 235 (2021).
11. Y. Meng, Z. Liu, Z. Xie, R. Wang, T. Qi, F. Hu, H. Kim, Q. Xiao, X. Fu, Q. Wu, S. H. Bae, M. Gong, and X. Yuan, Photonics Res. **8**, 564 (2020).
12. Z. Li, M. H. Kim, C. Wang, Z. Han, S. Shrestha, A. C. Overvig, M. Lu, A. Stein, A. M. Agarwal, M. Loncar, and N. Yu, Nat. Nanotechnol. **12**, 675 (2017).
13. B. Fang, H. Li, S. Zhu, and T. Li, Photonics Res. **8**, 1296 (2020).
14. X. Guo, Y. Ding, X. Chen, Y. Duan, and X. Ni, Sci. Adv. **6**, eabb4142 (2020).
15. Y. Ding, X. Chen, Y. Duan, H. Huang, L. Zhang, S. Chang, X. Guo, and X. Ni, ACS Photonics **9**, 398 (2022).
16. Y. Ha, Y. Guo, M. Pu, X. Li, X. Ma, Z. Zhang, and X. Luo, Adv. Theory Simul. **4**, 2000239 (2021).
17. K. Xi, B. Fang, L. Ding, L. Li, S. Zhuang, and Q. Cheng, Opt. Express **30**, 16699 (2022).
18. Y. Shi, C. Wan, C. Dai, S. Wan, Y. Liu, C. Zhang, and Z. Li, Optica **9**, 670 (2022).
19. B. Fang, Z. Wang, S. Gao, S. Zhu, and T. Li, Nanophotonics **11**, 1923 (2022).
20. Y. Shi, C. Wan, C. Dai, Z. Wang, S. Wan, G. Zheng, S. Zhang, and Z. Li, Laser Photonics Rev. **16**, 2100638 (2022).
21. C. Wan, Z. Li, S. Wan, C. Dai, J. Tang, Y. Shi, and Z. Li, Adv. Funct. Mater. **32**, 2110592 (2022).
22. R. Zhao, X. Xiao, G. Geng, X. Li, J. Li, X. Li, Y. Wang, and L. Huang, Adv. Funct. Mater. **31**, 2100406 (2021).
23. J. Jang, G. Lee, J. Sung, and B. Lee, Adv. Opt. Mater. **9**, 2100678 (2021).
24. R. Yang, Q. Yu, Y. Pan, S. Chen, C. Zhang, H. Ye, X. Zhou, Y. Shi, S. Wan, Y. Liu, and Z. Li, Opto-Electron. Eng. **49**, 220177 (2022).
25. A. D. Broadbent, Color Res. Appl. **29**, 267 (2004).